In Silico, in Vitro, and in Vivo Evaluation of New Candidates for α-Synuclein PET Imaging

Mathieu Verdurand, Élise Levigoureux, Waël Zeinyeh, Laurent Berthier, Meriem Mendjel-Herda, Florence Cadarossanesaib, Caroline Bouillot, Thibault Iecker, Raphaël Terreux, Sophie Lancelot, et al.

molecular pharmaceutics

Article

In silico, in vitro and in vivo evaluation of new candidates for alpha-synuclein PET imaging

Mathieu Verdurand, Elise Levigoureux, Wael Zeinyeh, Laurent Berthier, Meriem Mendjel-Herda, Florence Cadarossanesaib, Caroline Bouillot, Thibaut Iecker, Raphaël Terreux, Sophie Lancelot, Fabien Chauveau, Thierry Billard, and Luc Zimmer

Mol. Pharmaceutics, **Just Accepted Manuscript** • DOI: 10.1021/acs.molpharmaceut.8b00229 • Publication Date (Web): 10 Jul 2018

ACS Publications

is published by the American Chemical Society. 1155 Sixteenth Street N.W., Washington, DC 20036

In silico, *in vitro* and *in vivo* evaluation of new candidates for alpha-synuclein PET imaging

Mathieu Verdurand [£,≠], Elise Levigoureux [£,€,≠*], Wael Zeinyeh [£], Laurent Berthier [Ω], Meriem Mendjel-Herda [£], Florence Cadarossanesaib [¥], Caroline Bouillot [¥], Thibault Iecker [¥], Raphaël Terreux [Ω], Sophie Lancelot [£,€], Fabien Chauveau [£], Thierry Billard [¥,∞], Luc Zimmer [£,€,¥,]

[£] Université de Lyon, Université Claude Bernard Lyon 1, Lyon Neuroscience Research Center, CNRS UMR5292, INSERM U1028, Lyon, France.

[€] Hospices Civils de Lyon, Lyon, France.

[¥] CERMEP-Imaging Platform, Bron, France.

[∞] Université de Lyon, Université Claude Bernard Lyon 1, Institute of Chemistry and Biochemistry, CNRS UMR5246, Villeurbanne, France.

[Ω] Université de Lyon, Université Claude Bernard Lyon 1, Institute of Biology and Chemistry of Proteins, CNRS UMR5305, Lyon, France.

[≠] **Authors that contributed equally to this work**

* Corresponding author

Prof. Luc Zimmer

Email: Luc.Zimmer@univ-lyon1.fr

Phone: +33 4 72 68 86 09

Fax: +33 4 72 68 86 10

Short title: Towards alpha-synuclein PET neuroimaging

ABSTRACT

Accumulation of α-synuclein (α-syn) is a neuropathological hallmark of synucleinopathies. To date, no selective α-syn positron emission tomography (PET) radiotracer has been identified. Our objective was to develop the first original, selective and specific α-syn PET radiotracer.

Chemical design inspired from three structural families that demonstrated interesting α-syn binding characteristics was used as a starting point. Bioinformatics modelling of α-syn fibrils was then employed to select the best molecular candidates before their syntheses. An *in vitro* binding assay was performed to evaluate the affinity of the compounds. Radiotracer specificity and selectivity were assessed by *in vitro* autoradiography and *in vivo* PET studies in animal (rodents) models. Finally, gold standard *in vitro* autoradiography with patients' *post-mortem* tissues was performed to confirm/infirm the α-syn binding characteristics.

Two compounds exhibited a good brain availability and bound to α-syn and Aβ fibrils in a rat model. In contrast, no signal was observed in a mouse model of synucleinopathy. Experiments in human tissues confirmed these negative results.

KEYWORDS

Synucleinopathies; Parkinson's disease; multiple system atrophy; alpha-synuclein; radiotracer; positron emission tomography.

INTRODUCTION

Several neurodegenerative diseases share common pathological mechanisms whereby certain endogenous proteins (amyloid-beta or Aβ, alpha-synuclein or α-syn, Tau) form fibrillary aggregates composed of β-sheet structures that are linked with the pathological processes[1]. Among neurodegenerative proteinopathies, those characterized by α-syn protein aggregates form a heterogeneous group of diseases called "synucleinopathies". Alpha-synuclein aggregates are localized inside neurons in Parkinson's disease (PD), PD with dementia (PDD) and dementia with Lewy bodies (DLB), while they form oligodendroglial cytoplasmic inclusions in multiple system atrophy (MSA) [2].

International guidelines have highlighted a crucial need to develop tools for brain imaging in the diagnosis and follow-up of these diseases [3-5]. Positron emission tomography (PET) enables non-invasive *in vivo* and *in situ* visualization, characterization and quantification of physiological processes at cellular or molecular level. In the absence of early clinically relevant biomarkers, PET imaging of α-syn would allow better understanding of pathophysiological processes involving α-syn, differential and possibly pre-symptomatic diagnosis of synucleinopathies and, finally, evaluation of disease-modifying drugs targeting α-syn [6].

The development of a radiopharmaceutical specifically binding to α-syn aggregates raises numerous challenges: first in terms of sensitivity, as α-syn aggregates are present at lower density than Aβ aggregates *in vivo*; and second in terms of localization, as α-syn aggregates that are localized intracellularly and thus need a radiotracer able to cross the blood-brain barrier (BBB) and neuron or oligodendrocyte membranes. Last but not least, a successful radiotracer will have to be selective against the other proteins that also form β-sheets 3-dimensional (3D) structures: Aβ, Tau, TDP-43, and insulin. The most noticeable are amyloid Aβ aggregates, found in

Alzheimer disease (AD) but also in other neurodegenerative diseases, including synucleinopathies [7, 8]. Concurrently, the majority of DLB patients exhibit extensive cortical Aβ deposition [9]. This overlap complicates the quantification of PET images, pushing the PET imaging community to investigate in depth the precise selectivity of the radiotracers already developed and of those to come. In this regard, a particularly important and difficult point is to find one or several models (cell lines overexpressing α-syn, *in vitro* α-syn fibrils, transgenic animals overexpressing α-syn) that accurately reflect the aggregation process occurring in humans [10], knowing that the gold-standard will always be evaluation performed on human tissue and, ultimately, *in vivo* in patients.

All these challenges can explain that there is still no PET radiotracer available to measure α-syn protein brain accumulation. If the amyloid radioligand 5-[(E)-2-[6-(2-[18F]fluoroethoxy)-1,3-benzoxazol-2-yl]ethenyl]-N,N-dimethyl-1,3-thiazol-2-amine (BF227), radiolabeled with carbon-11 or fluorine-18, has demonstrated interesting binding properties to fibrils *in vitro* [11] and α-syn glial inclusions in MSA patients [12], these results have not been extended to α-syn accumulation in other synucleinopathies such as PD, PDD or DLB. Other lead compounds such as [^{125}I]SIL23, that bind selectively to α-syn *in vitro* [13], or [^{18}F]46a, with a higher selectivity for α-syn recombinant fibrils than for Aβ fibrils [14], all failed *in vivo*.

The aim of this study was thus to develop a PET radiotracer of aggregated α-syn proteins. The present study followed a rational and multidisciplinary approach to orient the design and the evaluation of α-syn PET radiotracer-candidates. Several steps were undertaken with, firstly, the chemical design of candidate molecules derived from three structural families that demonstrated interesting α-syn binding characteristics in the literature[11, 15-18]. The second step used bioinformatics modeling tools to model an α-syn fibril, propose an interesting docking site along the fibril, and evaluate the docking capabilities of our candidates toward this interaction site and

also their ability to reach the identified binding pocket. As a final step, the "best" candidates were synthesized, radiolabeled with fluorine-18, tested *in vitro*, evaluated by *in vitro/in vivo* imaging studies in several animal models and, ultimately, *post-mortem* on AD, PD, MSA patients' brains.

MATERIALS AND METHODS

Computational studies

Modelization of a-syn fibrils

The sequence of α-syn was obtained from the UniProt database. Using the Protein Data Bank structure 2MPZ as scaffold[19], mutations were made to replace the amino acids by the α-syn sequence. The resulting layer model was duplicated on the fibril axes, following beta-pleated conformation determined from a cryo-electron microscopy map (EMD-6482) [20], to obtain a final model composed of 18 layers. After energy minimization, the structure was processed in a 20 ns molecular dynamics simulation.

Identification of a docking site

Simulations were performed with AMBER software version 16. All simulations were performed in the conditions of a solution, using 5-site transferable interaction potential (TIP5P) as water model, and the system was neutralized with chloride ions (Cl^-). The periodic boundary condition was chosen as a parallelepiped with about 12 Å extension in all directions. The molecular simulation time step was set at 2 fs, with 300 K as final temperature and 1 atm as pressure, leading to the discrimination of different conformations. The binding sites were identified for these fibril structures, using the Site Finder program implemented in Molecular Operating Environment (MOE).

Evaluation of docking performance

All docking scores were performed with MOE 2014 in the interaction site determined using Site Finder and the best conformations of the complex were transferred to umbrella sampling simulations.

Ability to reach the identified docking site

Umbrella sampling simulations were performed with 220 windows, with distances between the center of mass of the tracer and the atoms of the protein ranging from 27 Å to 5.1 Å at 0.1Å intervals. In each window, a harmonic potential with 25 kcal/mol.$Å^2$ force constant was applied to maintain these previous distances. Also, positional restraints were applied to backbone atoms of the two proteins which are at the edge of the fibril and the atoms of the protein concerned by the reaction coordinate. For each window, we performed a simulation of 40 ps duration for equilibration and 100 ps duration for production, with data collection every 50 fs at 300 K and 1 atm. Finally, the weighted histogram analysis method was employed to reconstruct the free energy profile along the reaction coordinate from the biased probability distribution of each window.

Chemical syntheses

These syntheses are showed in Figure 1.

Synthesis of tert-butyl N-{4-[(E)-2-(1,3-benzoxazol-2-yl)ethenyl]phenyl}-N-methylcarbamate (3)

To a solution of **1** (0.435 mL, 3.70 mmol) and **2** (0.725 g, 3.08 mmol) in THF / tert-butanol (30 mL / 1.8 mL), cooled at 0°C, was added potassium tert-butoxide (0.442 g, 4.01 mmol). After 1h at 0°C, the reacting mixture was stirred overnight at room temperature. Then, a saturated aqueous solution of $NaHCO_3$ was added, followed by extraction with ethyl acetate. Organic phase was then washed with brine and dried over $MgSO_4$. After evaporation, purification by flash

chromatography (eluent: pentane/ethyl acetate, 90:10) was performed to obtain **3**, as a yellow solid (0.843 g, 78 %).

^{1}H NMR ($CDCl_3$, 300MHz): δ 7.86 (d, 1H, *J*=16.2Hz), 7.80-7.70 (m, 1H), 7.62-7.51 (m, 3H), 7.40-7.28 (m, 4H), 7.08 (d, 1H, *J*=16.2H), 3.30 (s, 3H), 1.48 (s, 9H).

Synthesis of 4-[(E)-2-(1,3-benzoxazol-2-yl)ethenyl]-N-methylaniline hydrochloride (4)

To a solution of **3** (0.82g, 2.34 mmol) in $CH_éCl_é$ (19 mL), cooled at 0°C, was added trifluoroacetic acid (1.9 mL). The solution was stirred at 0°C for 4h an, then, the solvents were evaporated in vacuo and the rsulting mixture was extract with ethyl acetate and saturated aqueous solution of $NaHCO_3$. The organic phase is washed with brine and dried over Na_2SO_4. After evaporation, THF and HCl (37%) were added. The precipitated solid was filtered and washed with THF. All the resulting organic phases were neutralized with a saturated aqueous solution of $NaHCO_3$. After evaporation, the resulting mixture was then extracted with ethyl acetate. The organic phase was then evaporated and HCl (37%) is added to form another precipitate. All the obtained solids were combined to afford **4**, as a yellow solid (0.551 g, 82%).

^{1}H NMR (CD_3OD, 300MHz): δ 7.93-7.81 (m, 3H), 7.73-7.60 (m, 2H), 7.49-7.35 (m, 4H), 7.21 (d, 1H, *J*=16.3H), 3.07 (s, 3H).

Synthesis of N-{4-[(E)-2-(1,3-benzoxazol-2-yl)ethenyl]phenyl}-4-fluoro-N-methylbenzene-1-sulfonamide (4FBox)

To a solution of **4** (0.128 g, 0.45 mmol) and 4-fluorobenzenesulfonyle chloride (0.088 g, 0.45 mmol) in anhydrous CH_2Cl_2 (7 mL), colled at 0°C, was added trimethylamine (0.155 mL, 1.12 mmol). The reacting mixture is then stirred at room temperature for 24h. After evaporation of solvents, the resulting mixture was dissolved with CH_2Cl_2 and washed with an aqueous solution

of $KHSO_4$ (5%) and then with brine. After purification with flash chromatography (CH_2Cl_2 / diethyl ether), **4FBox** (0.1 g, 55%) was obtained as a yellow solid.

^{1}H NMR (DMSO-d_6, 400MHz): δ 7.84-7.77 (m, 3H), 7.76-7.69 (m, 2H), 7.63-7.57 (m, 2H), 7.47-7.35 (m, 4H), 7.33 (d, 1H, *J*=16.4Hz), 7.23-7.18 (m, 2H), 3.17 (s, 3H).

^{13}C NMR (DMSO-d_6, 100MHz): δ 164.7 (d, *J*=252 Hz), 162.6, 149.8, 142.0, 141.7 138.3, 133.6, 132.1 (d, *J*=2.7 Hz), 130.5 (d, *J*=9.8 Hz), 128.5, 126.2, 125.6, 124.8, 119.6, 116.6 (d, *J*=23.0 Hz), 114.4, 110.6, 37.6.

^{19}F NMR (DMSO-d_6, 282MHz): δ -105.91.

Synthesis of N-{4-[(E)-2-(1,3-benzoxazol-2-yl)ethenyl]phenyl}-2-fluoro-N-methylbenzene-1-sulfonamide (2FBox)

Similar procedure to **4FBox** with 2-fluorobenzenesulfonyle chloride. **2FBox** is obtained as yellow solid (0.1 g, 64%).

^{1}H NMR (DMSO-d_6, 400MHz): δ 7.83-7.63 (m, 7H), 7.51-7.25 (m, 7H), 3.29 (d, *J*=1.3 Hz, 3H).

^{13}C NMR (DMSO-d_6, 100MHz): d 162.3, 158.1 (d, *J*=254.9 Hz), 149.8, 141.69, 141.65, 138.3, 136.3 (d, *J*= 8.6Hz), 133.5, 130.9, 128.5, 125.9, 125.6, 125.1 (d, *J*=3.6 Hz), 124.8, 124.6 (d, *J*=14.6 Hz), 119.6, 117.6 (d, *J*=21.5 Hz), 114.3, 110.6, 37.6 (d, *J*=2.8 Hz).

^{19}F NMR (DMSO-d_6, 282MHz): δ -108.61.

Synthesis of N-{4-[(E)-2-(1,3-benzoxazol-2-yl)ethenyl]phenyl}-N-methyl-4-nitrobenzene-1-sulfonamide (4NBox)

Similar procedure to **4FBox** with 4-nitroobenzenesulfonyle chloride. **4NBox** is obtained as yellow solid (0.145 g, 87%).

^{1}H NMR (DMSO-d_6, 400MHz): δ 8.43-8.37 (m, 2H), 7.85-7.78 (m, 5H), 7.76-7.70 (m, 2H), 7.44-7.38 (m, 2H), 7.35 (d, 1H, *J*=16.4Hz), 7.25-7.21 (m, 2H), 3.23 (s, 3H).

^{13}C NMR (DMSO-d_6, 100MHz): δ 162.2, 150.1, 149.8, 141.7, 141.5, 141.2, 138.3, 134.0, 129.0, 128.6, 126.6, 125.6, 124.8, 124.6, 119.7, 114.6, 110.6, 37.9.

Synthesis of N-{4-[(E)-2-(1,3-benzoxazol-2-yl)ethenyl]phenyl}-N-methyl-2-nitrobenzene-1-sulfonamide (2NBox)

Similar procedure to **4FBox** with 2-nitroobenzenesulfonyle chloride. **2NBox** is obtained as yellow solid (0.07 g, 42%).

^{1}H NMR (DMSO-d_6, 400MHz): δ 8.00 (dd, *J* = 8.0 Hz, 1.1 Hz, 1H), 7.92 (td, *J* = 7.7 Hz, 1.1Hz, 1H), 7.88-7.68 (m, 7H), 7.45-7.29 (m, 5H), 3.33 (s, 3H).

^{13}C NMR (DMSO-d_6, 100MHz): δ 162.2, 149.8, 147.9, 141.7, 141.2, 138.3, 135.2, 134.0, 132.3, 130.4, 129.0, 128.7, 126.7, 125.6, 124.8, 124.3, 119.7, 114.6, 110.6, 38.4.

Radiolabeling of [^{18}F]BF227, [^{18}F]2FBox and [^{18}F]4FBox

Fluorine–18 was obtained via the ^{18}O (p,n)^{18}F reaction (IBA Cyclone18/9 cyclotron). Fluoro substitution of the precursor was performed on a standard Neptis® synthesizer (ORA™): after initial fluoride preparation (collection, drying and Kryptofix activation), 1.0-2.0 mg radiolabeling precursor of [^{18}F]BF227, [^{18}F]2FBox or [^{18}F]4FBox was introduced and the reaction mixture was heated at 150°C for 10 min in DMSO (**Figure 2**). The reaction mixture was passed through an activated C18 cartridge for pre-purification and the crude product was eluted from the cartridge with methanol. Pure [^{18}F]BF227 was obtained after separation on a preparative high-performance liquid HPLC. For biological use, the product was diluted with sterile water, loaded onto a C18 cartridge (SEP-Pak Light, Waters), eluted with ethanol and diluted with isotonic saline to an ethanol concentration of 5%. Quality control of [^{18}F]BF227, [^{18}F]2FBox or [^{18}F]4FBox consisted in determining radiochemical purity and specific activity, by analytic HPLC assay (UV and

radioactive detections). The identity of [^{18}F]BF227, [^{18}F]2FBox or [^{18}F]4FBox was confirmed by co-injection with an authentic non-radioactive sample.

Screening material

Preparation of fibrils. Lyophilized α-synuclein (α-syn) protein and amyloid-β 1-42 (Aβ42) peptide (recombinant human proteins, rPeptide®) were dissolved in water for injection (WFI) with 0.02% azide to a final concentration of 200 µM. The solutions were incubated at 37°C with constant agitation at 250 rpm using a thermomixer (Thermo-Shaker PHnT, Grant-bio®). Fibril aggregation was confirmed through thioflavin S (ThS) fluorescence staining.

Injected rats. In order to evaluate both the ability of radiotracer candidates to cross the blood brain barrier and to dectect α-syn and Aβ1-42 fibrils, a model of rat was designed. These animals constitute robust and easy to implement and control animal model of proteinopathies. Adult male Sprague-Dawley rats (8-9 weeks old) weighing 250-400 g were used (Charles River Laboratories, L'Arbresle, France). All animal experiments were performed in accordance with the European guidelines (2010/63/UE) and were approved by the Animal Use Ethics Committee of the University of Lyon (C2EA-42; Comité d'Ethique en Expérimentation Animale Neurosciences Lyon; celyne.lyon@inserm.fr). Rats were anesthetized with isoflurane inhalation in air (4% isoflurane in 1 L/min air) and then transferred to a stereotaxic apparatus (Stoelting, USA) equipped with a mask delivering isoflurane at 1.25%-2.5% for the duration of the experiment. Body temperature was maintained by a heating pad set at 37°C and monitored rectally. A pulse oximeter was used to measure heart rate, respiratory rate and oxygen saturation. Pain was controlled by the potent opioid analgesic buprenorphine (Buprecare, Axience) injected subcutaneously at a dose of 0.05 mg/kg 20 minutes before any surgical act was performed. Animals (n=7) were stereotaxically injected (1 nmol in 5 µL per injection site) with pre-

aggregated Aβ1-42 at the level of the caudate putamen (CPu) and α-syn in the contralateral CPu, randomly (stereotaxic coordinates relative to bregma: AP = -3.2 mm; ML = ± 1.2 mm; DV = -3.6 mm), according to the stereotaxic atlas of the rat brain [21]. Fibrils were slowly infused at a constant rate of 1 µL/min with 30-gauge needles. The needles were left in place for 2 minutes and then slowly withdrawn. After injections, the scalp was sutured, an antiseptic (povidone-iodine) and local analgesic (lidocaine) were applied, and the rats were allowed to recover from anesthesia. A 7-day post-injection interval was observed before euthanasia and subsequent studies.

Transgenic mice. The "accelerated" version of the transgenic (Tg) mouse model (M83) expressing human A53T mutated α-syn was used [22]. In this accelerated model, α-syn aggregates appear ~100 days after inoculation, especially in the brainstem and midbrain [22]. This period corresponded to the age of animal used for *in vitro* autoradiography brain sections. C57Bl/6S brain sections of a mouse presenting a deletion of the α-syn locus (α-syn KO) (Harlan, Gannat, France) were used as control. The transgenic mouse model (PDAPP line J20), overexpressing 2 human mutations of APP genes [23], was obtained from collaborators (Dr N. Rama, CRCL, UMR INSERM 1052, CNRS 5286, Lyon). Animal brain sections were used when they expressed large Aβ plaques in hippocampus and cortex.

Human postmortem brains. Human brain tissue sections were obtained as frozen sections from London Neurodegenerative Diseases Brain Bank and a local brain bank in Lyon (Cardiobiotec, HCL). Consecutive medulla sections from patients with various synucleinopathies were used for *in vitro* autoradiography. These included one PD patient (79 year-old male), one MSA patient (71 year-old male) and one control patient (63 year-old female). Consecutive brain sections, at the level of cortex and hippocampus, from one AD patient (67 year-old male) were also included in the *in vitro* autoradiography experiments.

In vitro binding assay

Synthetic α-syn and Aβ42 fibrils (200 nM) were incubated with increasing concentrations of radiotracer (0.5-200 nM). In order to evaluate the non-specific binding of the compounds, the below-mentioned reactions were performed in the presence of 50 μM unlabeled compound. Samples were incubated for 1 hour at room temperature in 200 μL assay buffer (phosphate buffer saline: PBS, 0.1% bovine albumin serum: BSA). Bound radiolabeled tracer was separated from free tracer by filtration under reduced pressure (Multiscreen HTS Vacuum Manifold; Multiscreen HTS-FB 1.0/0.65μm, Millipore). Filters were washed three times with 200 μL PBS. Washed filters were assayed for radioactivity by gamma counter (Gamma Wizard 2480-160715, Perkin Elmer). Binding data were analyzed with curve-fitting software that calculated Kd and Bmax on non-linear regression (GraphPad Software, Prism 5). All experiments were conducted in triplicate.

In vivo small-animal PET imaging

Fibril-injected (n=5) and non-injected control rats (n=5) were used for *in vivo* PET imaging experiments in isoflurane-anaesthetized animals (4% induction and 2% maintenance). Each experiment was performed in duplicate for each group (fibril-injected vs non-injected) and for each radiotracer ([^{18}F]BF227, [^{18}F]2FBox, and [^{18}F]4FBox). PET scans were acquired in list mode, using a Siemens INVEON PET/CT scanner, with a nominal in-plane resolution of ~1.4 mm full-width-at-half-maximum in the center of the FOV. A 60-minute list mode acquisition started immediately after caudal intravenous injection of [^{18}F]BF227, [^{18}F]2FBox or [^{18}F]4FBox. The reconstructed images led to a volume of 159 slices of 128 x 128 voxels, with voxel size

0.388 x 0.388 x 0.796 mm. The dynamic images obtained were analyzed on the INVEON Research Workplace (IRW, Siemens).

PET was co-registered with CT, and both were co-registered with our in-house rat MRI atlas [24], to extract radioactivity values in the whole brain (general brain uptake) but also in the region of interest (ROI), the CPu, where the fibrils were injected. Time activity curves (TAC) were expressed as percentage of injected dose per gram (%ID/g) and standardized uptake values (SUV) [25] over time. SUV summed over the 40-60 min. period (where TAC plateaued) were also calculated at the fibril-injected sites (CPu) and divided by the SUV measured in an area devoid of fibrils (cerebellum (Cb)) to give an index of radiotracer uptake (SUV ratio = SUVR = $[SUV_{CPu}]$ / $[SUV_{Cb}]$).

***In vitro* autoradiography**

Animals (fibril-injected rats and transgenic mice) were deeply anesthetized with isoflurane in the inducing chamber (4% isoflurane in 1 L/min air flow) and rapidly euthanized by decapitation. Brains were dissected and frozen in 2-methylbutane with dry ice (-30°C). Thirty-micrometer sections were cut across the respective ROIs: coronal CPu sections for fibril-injected rats, sagittal sections encompassing midbrain and brainstem for M83 mice, and sagittal sections through hippocampus and cortex for PDAPP transgenic mice. Sections were then thaw-mounted on slides (Superfrost®, Roth, France) and allowed to air-dry for 30 minutes before storage at -80°C until use. On the day of tracer synthesis, the slides (animal and human postmortem) were allowed to thaw at RT for 30-60 minutes and sections were incubated at RT for 30 minutes in Tris-buffered saline (TBS) supplemented with HCl (TBS-HCl buffer) (138 mM NaCl, 2.7 mM KCl, pH adjusted to 7.5) containing 37 kBq/mL of either [^{18}F]BF227, [^{18}F]2FBox or [^{18}F]4FBox. After incubation, slides were dipped twice in an 8:1 ethanol/water mixture at RT for 1 minute then

dried under cool air, and exposed on a sensitive phosphor imaging plate BAS-IP MS 2025, Fujifilm) overnight. The distribution of radioactivity was then qualitatively visualized on a Bio-imaging analyser system (BAS-5000, Fujifilm).

Immunofluorescence

The frozen sections used for *in vitro* autoradiography or adjacent frozen brain sections were used for immunofluorescence studies. Brain sections were post-fixed in 4% paraformaldehyde in PBS for 20 minutes followed by 3 PBS washes of 5 min each, and transferred to a PBS solution (0.02% azide) at 4°C until use. An antigen retrieval/unmasking step was conducted with 99% formic acid solution for 10 min followed by 3 PBS washes of 5 min each. Slides were then dipped in blocking and permeabilization buffer (PBST with 5% BSA and 0.5% Triton X-100) for 30 min followed by 3 PBS washes of 5 min each. Incubation in PBST containing primary antibodies was then performed overnight at 4°C. The primary antibodies used were 4G8 clone for Aβ (1/1000; anti-β-amyloid, 17-24 antibody, mouse IgG2b), or 5G4 clone for α-syn (1/1000; anti-aggregated a-synuclein, monoclonal mouse IgG1κ). Slides were then incubated in PBST containing the secondary antibody Alexa Fluor 594 (1/1000; AF594 anti-mouse, LifeTechnologies) for 1 hour at room temperature followed by 3 PBS washes of 5 min each. Alternatively to immunofluorescence, thioflavin-S staining was performed with 0.0025%.

Fluorescence was first observed using an imaging microscope (Axioplan-2, Zeiss; Oberkochen, Germany). A Texas Red (ex 587 ± 25 nm, em 647 ± 70 nm) filter was used for AF594 secondary antibody and a GFP (ex 470 ± 40 nm, em 525 ± 50 nm) filter for ThS. Images were captured using a digital camera interfaced with image-analysis software (Axiovision 3.0 software, Zeiss). Fluorescence was then observed and captured with a digital slide scanner (Axio Scan.Z1, Zeiss) (CIQLE Imaging Platform, University of Lyon, France) equipped with similar

filters, in order to have a full view and digital image of each brain section. For human postmortem immunofluorescence images, the green channel (non-specific auto-fluorescence binding) was subtracted (Adobe Photoshop CS6 tool) from the red channel in order to obtain images with only red specific immunolabeling.

RESULTS

Chemical Design

The chemical design of ten candidate molecules derived from three structural families that demonstrated moderate to high affinity towards α-syn fibrils, and modified to be easily radiolabeled with fluorine-18, were explored.

The first structural family consisted of tricyclic antidepressants that were mentioned in a patent that demonstrated an interesting binding of imipramine and nortyptilline towards a-syn fibrils[15]. Five fluorinated compounds (4FN, 2FN, 4FD, 2FD, F2CN) were drawn (**Figure 3A**).

Inspired by the structure of the dyes used in histochemistry to reveal the α-syn aggregates in *post-mortem* studies, and from whom BF227 was derived[11], the second family consisted of benzoxazoles derivatives. The benzoxazole-vinyl cores were conserved with the aim to reproduce and improve these binding properties (**Figure 1**). The pharmaco-modulation focused on the amino-thiazole part which was substituted by an amino-benzene moiety. A benzene sulfonyl part was also added on the amino function to allow a subsequent facilitated radiolabeling with fluorine-18. These structures have a poly-conjugated planar structure interesting for interactions with β-sheet structures of α-syn fibrils. Two candidate molecules were developed: 2FBox and 4FBox (**Figure 3B**).

The last series of molecules were derived from benzimidazoles derivatives which demonstrated moderate α-syn binding affinity but 2-3 fold higher selectivity towards α-syn in comparison to

amyloid-β aggregates[16-18]. Some of these compounds having demonstrated a E/Z double-bond isomerization,[13] the central double bonds were replaced by a triple bond to conserve the conjugation of the structure without isomerization abilities. With their planar structure, these benzimidazoles derivatives present promising conformation in order to bind (through π-π interactions) to the channels formed along the β-sheets fibrils/filaments. Three candidate molecules were developed and included F4SBiYB, F3CBiYB and F2PBiYB (**Figure 3C**).

Computational modeling, docking site identification and accessibility

Modelization of the a-syn fibrils

The sequence of α-syn was obtained from the UniProt database (www.uniprot.org) under the reference P37840-1. Modeling of α-syn fibril structure was based on a cryo-electron microscopy (cryo-EM) study [20] and consisted in a fragment of α-syn fibrils with two entwined, asymmetrically associated protofibrils. A portion of α-syn fibril with 36 α-syn proteins (18 layers of duplicated α-syn proteins) was reproduced in all-atoms resolution. After a molecular dynamic of 20 ns in the isothermal-isobaric ensemble, 5 representative conformations of the fibril were sampled by 2D-RMSD (root mean square deviation), in which a common interaction site was identified by Site Finder. This site was oriented parallel to the fibril axis, located between amino-acids 67 and 75 of the α-syn protein, and formed a loop in the fibril (**Supplementary Figure S.A1**).

Docking scores

Computation of docking simulations gave a score evaluating the affinity of all our 10 candidate molecules for the identified docking site (with the highest pseudo-affinities for the lowest numerical values). The tricyclic antidepressant family was the one that showed, overall, the less interesting docking scores (**Table 1**). The benzimidazoles derivatives' docking scores varied

from -5.0 kcal/mol to -6.9 kcal/mol. The benzoxazoles derivatives were the ones with the highest docking scores towards the identified α-syn binding pocket with an improved docking score in comparison to BF227 (docking score for 4FBox = -9.0 kcal/mol, 2FBox = -8.7 kcal/mol and BF227 = -8.3 kcal/mol). The docking results showed that the chemical modifications brought to BF227 derivatives' 2FBox and 4FBox were not predicted to annihilate their binding to the α-syn fibril.

Structural Families	Candidate Molecules	α-syn fibril docking scores (kcal/mol)
Tricyclics	4FD	-4,3
	2FN	-3,9
	4FN	-3,5
	2FD	-3,4
	F2CN	-3,2
Benzoxazoles	4FBox	-9,0
	2FBox	-8,7
additional info	*BF227*	*-8,3*
Benzimidazoles	F3CBiYB	-6,5
	F2PBiYB	-6,4
	F4SBiYB	-5,0

Table 1. Docking scores of our candidate molecules towards the identified docking site on the α-syn fibril model. Values are expressed in kcal/mol and reflect pseudo-affinities (the highest pseudo-affinities for the lowest values). Scores presented are GBVI/WAS (Generalized-Born Volume Integral/Weighted Surface Area).

Ability to reach the docking site

Umbrella sampling calculations (highly demanding in terms of computing power) were only performed for the two candidate molecules that demonstrated the highest docking scores towards the α-syn binding pocket, namely, 2FBox and 4FBox. The identified radiotracer interaction site was deeply buried within the α-syn structure. Candidate molecules must thus penetrate the structure between strand ladders to reach the interaction site. In order to simulate and calculate an energy profile for the whole access process, umbrella sampling simulations were performed. Calculation speed was enhanced by extracting a fragment of 13 α-syn proteins in which the sequence was reduced to amino-acids 35-91. The potential of mean force results (PMF) graphical illustration is the umbrella sampling method we chose to reflect the accessibility of our candidate molecules to the interaction site (**Supplementary Figure S.1B**). The energetic barrier was the highest for 2FBox (7.1 kcal/mol), intermediate for 4FBox (6.5 kcal/mol) and the lowest for BF227 (6 kcal/mol). PMF for 4FBox and 2FBox showed similar profiles and penetration patterns.

Candidate molecules and radiolabeling

Synthesis of non-radioactive FBox compounds and their precursors for radiolabeling

The non-radioactive FBox compounds and their precursors for radiolabeling (NBox) were synthesized following a divergent strategy (**Figure 1**). The common intermediate **4** was obtained from the reaction between 2-methylbenzoxazole (**1**) and aldehyde **2**, followed by Boc deprotection of the obtained compound **3**. The FBox molecules could be then obtained through reaction with the corresponding fluorobenzenesulfonyl chloride (ortho-substituted for N-{4-[(E)-2-(1,3-benzoxazol-2-yl)ethenyl]phenyl}-2-[18F]fluoro-N-methylbenzene-sulfonamide (2FBox) and para-substituted for N-{4-[(E)-2-(1,3-benzoxazol-2-yl)ethenyl]phenyl}-4-[18F]fluoro-N-methylbenzenesulfonamide (4FBox)). Similarly, NBox compounds were formed from the corresponding nitrobenzenesulfonyl chloride (ortho-substituted for N-{4-[(E)-2-(1,3-benzoxazol-

2-yl)ethenyl]phenyl}-N-methyl-2-nitrobenzenesulfonamide (2NBox) and para-substituted for N-{4-[(E)-2-(1,3-benzoxazol-2-yl)ethenyl]phenyl}-N-methyl-4-nitrobenzenesulfonamide (4NBox)). The overall yields of these 3-step syntheses were generally satisfactory to good.

The radiolabeled compounds were obtained successfully through nucleophilic substitution of nitro group from 4NBox and 2NBox, with satisfactory radiochemical yields (10-19%) (**Figure 2**). Specific activity (SA) was relatively high (range, 68-543 GBq.µmol^{-1}) for our 2 tracers. The logD values were in accordance with good permeation of brain blood barrier (Figure 2).

***In vitro* radioactive saturation assays**

[^{18}F]BF227, [^{18}F]4FBox and [^{18}F]2FBox selectivity were tested against synthetic α-syn and Aβ42 fibrils. First, successful formation of fibrils from recombinant proteins[26] was determined by thioflavin S staining and direct observation of fibrils from recombinant proteins by transmission electronic microscopy (**Supplementary Figure S.2**). According to the literature[11], for [^{18}F]BF227, Kd was equal to 14.03 ± 43.52 nM and Bmax = 11.98 ± 9.49 pmol/nmol of fibrils for α-syn fibrils. For Aβ42 fibrils, Kd_1 was equal to 0.82 ± 1.08 nM and $Bmax_1$ = 0.91 ± 0.41 pmol/nmol of fibrils while Kd_2 was equal to 125.2 ± 29.05 nM to Aβ 1-42 and $Bmax_2$= 14.43 ± 10.07 pmol/nmol of fibrils (**Supplementary Figure S.3**). [^{18}F]4FBox bound with low affinity to α-syn fibrils (Kd = 155.4 ± 96.5 nM and Bmax = 2.073 ± 0.821 pmol/nmol of fibrils) and with better affinity to Aβ42 fibrils (Kd = 7.7 ± 2.6 nM and Bmax = 0.802 ± 0.070 pmol/nmol of fibrils, **Figure 4 C and D**). In contrast, [^{18}F]2FBox bound α-syn fibrils with high affinity (Kd = 3.3 ± 2.8 nM and Bmax = 0.128 ± 0.025 pmol/nmol of fibrils, and with lower affinity to Aβ42 fibrils (Kd = 145.3 ± 114.5 nM and Bmax = 0.592 ± 0.251 pmol/nmol of fibrils).

***In vitro* autoradiography in rats and mice**

In the striata of fibril-injected rats, all three radiotracers were able to non-selectively detect α-syn and Aβ42 synthetic fibrils in autoradiography experiments, as shown by intense radioactive signal located on the site where immunofluorescence confirmed the presence of aggregated α-syn and Aβ42 fibrils (**Figure 5**).

In the midbrain and brainstem of the Tg mouse model overexpressing a mutated form of α-syn (M83) and in the cortex and hippocampus of the Tg mouse model overexpressing 2 mutated forms of APP (PDAPP line 20), none of the three radiotracers were able to detect the α-syn or Aβ aggregates stained with ThS (**Figure 5**). The Tg mouse model lacking α-syn expression, as confirmed by absence of ThS staining, gave a similar negative radioactive signal (**Figure 5**).

***In vivo* PET imaging in rats**

PET imaging study was performed in our rat model, which exhibit α-syn on one side and Aβ 1-42 fibrils on the other side of the caudate putamen, compared to non-injected rat. The 60-minute acquisition started immediately after caudal intra-venous injection of [^{18}F]BF227 (10.9 ± 5.5 MBq; range, 7.4-17.2 MBq), [^{18}F]2FBox (12.4 ± 1.8 MBq; range, 10.8-14.9 MBq), or [^{18}F]4FBox (9.4 ± 6.6 MBq; range, 4.7-14.1 MBq). Biological evaluation of the three radiotracers indicated crossing of the blood-brain barrier and entry to the brain (**Figure 6**). Initial whole-brain uptake was higher and faster with [^{18}F]BF227 (0.65 %ID/g peak at 2 minutes post-injection) than with [^{18}F]4Fbox (0.47 %ID/g peak at 10 minutes p.i.) or [^{18}F]2FBox (0.47 %ID/g peak at 12 minutes p.i.). Standardized uptake values (SUV) approximating 2 at peak are usually desirable for PET brain radiotracers [27]. Calculated SUV at peak was close to 2, with values of 2.7, 1.6 and 1.6 for [^{18}F]BF227, [^{18}F]4FBox and [^{18}F]2FBox, respectively. Washout kinetics was moderate, with half of overall brain activity (calculations performed on the whole brain activity) still present after 60 min (5min/60min ratio: 2.2 for [^{18}F]BF227, 1.7 for [^{18}F]2FBox, 1.5 for

[^{18}F]4FBox). Injected fibrils were not detected by any of the three radiotracers *in vivo* (**Figure 6**). Calculated SUVR (mean ± SD) with [^{18}F]BF227 was 1.05 ± 0.03, 1.10 ± 0.12 and 1.05 ± 0.02 in control, Aβ42 and α-syn-injected striata, respectively. PET imaging with [^{18}F]2FBox gave SUVR = 1.08 ± 0.02, 1.13 ± 0.04 and 1.10 ± 0.02 in control, Aβ42 and α-syn -injected striata, respectively. Finally, [^{18}F]4FBox did not perform better, with SUVR (mean ± SD) of 1.12 ± 0.03, 1.05 ± 0.06 and 1.07 ± 0.05 in control, Aβ42 and α-syn -injected striata, respectively.

In vitro autoradiography in *post-mortem* patients' brain

In human *post-mortem* PD brain (medulla oblongata), none of the three radiotracers were able to image Lewy bodies or neurites, as seen from the absence of radioactive signal in these α-syn rich regions immunostained by 5G4 antibody, which preferentially labels aggregated synuclein [28] (**Figure 7**). In human *post-mortem* MSA brain where glial cytoplasmic α-syn inclusions were immunostained by 5G4, no radioactive signal could be detected with any of the three radiotracers (**Figure 7**). Similarly, in control human *post-mortem* brain, no radioactive signal or immunostaining could be detected (**Figure 7**). In human *post-mortem* AD brain, large Aβ plaques were immunostained by 4G8 antibody in the cortex and hippocampus. The [^{18}F]BF227 signal clearly co-localized with 4G8 staining and binding was displaced with non-radioactive BF227 in excess (data not shown). However, neither [^{18}F]2FBox nor [^{18}F]4FBox were able to detect Aβ plaques (**Figure 7**).

DISCUSSION

The development of an α-syn PET radiotracer is particularly challenging as indicated by the fact that all published attempts were failures. This general observation incited us to propose a slightly

different screening paradigm to evaluate our PET candidates. Starting from a "classical" chemical design of candidate molecules derived from three structural families that demonstrated interesting α-syn binding characteristics, we then developed a bioinformatics modelization approach (modelization of α-syn fibrils, identification of docking site, evaluation of candidate molecules docking scores and ability to reach the binding pocket) to select the "best" candidates and confirm the chemical choice before embarking in synthesis and radiolabeling, *in vitro* assays performed with synthetic fibrils, *in vitro*/*in vivo* imaging studies with animal models and, finally, *in vitro post-mortem* autoradiography studies.

From the design of 10 candidate molecules derived from three structural families, our objective was that this pharmaco-modulation could bring interesting selectivity and specificity properties towards α-syn fibrils. The cryo-EM α-syn fibril model we used for subsequent computational modeling was relevant because fibrils are known to be composed of multiple protofibrils [29, 30]. Even if a recent α-syn fibril NMR structure has been characterized [31], our model remained relevant as the NMR structure does not consider associations of multiple protofibrils. A recent study on Aβ styrylbenzoxazole candidate radiotracers showed that there was only a weak correlation between docking scores and experimental binding affinities[32]. Therefore, our docking results only gave indications (no definitive answers) on which structural families were more interesting. The tricyclic antidepressants and benzimidazoles structural families were the less interesting, with low docking scores. However, the chemical modifications brought to BF227's structure to produce our benzoxazoles derivatives 2FBox and 4FBox did not result in a drop/fall in the docking scores. Overall, our computational modeling experiments suggested that these last two candidate molecules retained a binding ability similar to BF227 (docking scores), though at the price of greater energy required to reach the binding site (umbrella sampling). We thus decided to attempt their radiolabeling with fluorine-18, and succeeded.

Consecutive saturation filter binding assays with recombinant synthetic fibrils showed that [^{18}F]2FBox was clearly the best of our two candidates. In our experimental conditions, [^{18}F]2FBox detected ~16-fold less binding sites (Bmax) on α-syn fibrils than [^{18}F]4FBox but it did so with a ~47-fold better affinity (Kd) and a nearly 44-fold selectivity towards α-syn versus Aβ42 fibrils, when [^{18}F]4FBox was more selective towards Aβ42 than α-syn fibrils (~20-fold). These results should nonetheless be interpreted with caution, as reproducibility issues were encountered. Though filter binding assay is a robust technique for "receptology", it might be less well adapted to fibrils, a very different type of target, which consequently generated non-specific, non-saturable binding in our experiments. Indeed, cerebral aggregates and synthetic fibrils display a high propensity to coat to surfaces [33, 34]. Another confounding feature of protein aggregates is their so-called structural polymorphism [35-37], the formation of several types of fibril, distinguished by variable 3D structures (differences in folding in the formation of folded β-sheets) and variable quaternary structures. These conformational changes could lead to different binding sites on these fibrils for candidate radiotracers. An aggregation polymorphism was observed by electronic microscopy: a modification of pH or of aggregation time showed formation of fibrils with different structures (data not shown). This heterogeneity of structure may be the source of significant variability in binding experiments, but it is also an opportunity for exploration with molecular imaging and computational modeling.

Evaluation in synthetic-fibril-injected rats demonstrated the ability of our radiotracers to non-selectively detect Aβ42 and α-syn recombinant human fibrils *in vitro* and *ex vivo* (data are presented in **Supplementary Figure S.4**). However, *in vivo* small-animal PET imaging in this same rat model showed that both radiotracers failed to detect either Aβ42 or α-syn fibrils despite good uptake in cerebral tissue. This discrepancy between *in vivo* and *in vitro* results is probably due in part to the low spatial resolution of small-animal PET imaging [38] in comparison to *in vitro*

autoradiography [39]. Low specific activity is another potential factor that has previously been implicated in the failure to detect Aβ plaques in animal models of AD [40-42]. However, in the present study, specific activity was unlikely to be responsible for non- detection *in vivo*, as specific activity (SA) was relatively high (range, 68-543 GBq.μmol^{-1}) for both tracers.

Similarly, [^{18}F]2FBox and [^{18}F]4FBox were unable to detect Aβ or α-syn in transgenic mouse models of Alzheimer's (PDAPP) and Parkinson's (M83) disease. [^{18}F]BF227, a derivative of a well-known carbon-11 Aβ radiotracer [43, 44], was not able to image either α-syn, as previously demonstrated by our team [45] or, more surprisingly, Aβ plaques. Hypotheses for this lack of Aβ plaques binding include methodological issues. It is known in PET imaging that radiotracer binding with good imaging contrast is a function of target-site density (Bmax; higher is better) relative to radiotracer affinity to the binding site (Kd; lower is better) [46]. It may be that the density of α-syn and Aβ plaque inclusions in these models were too low to achieve a good PET imaging contrast [45]. Concerning our candidate α-syn radiotracers, in the "PD-like" accelerated Tg mouse model (M83) expressing the human A53T mutated α-syn [22], neither [^{18}F]2FBox nor [^{18}F]4FBox were able to detect α-syn aggregates. Similarly, in the Tg mouse model (PDAPP line J20) overexpressing 2 human mutations of APP genes [23], [^{18}F]2FBox and [^{18}F]4FBox were not able to image the confirmed presence of Aβ plaques. These negative results obtained with transgenic mice models that overexpress human forms of the fibrils highlight the first "gap" between the feasibility of imaging synthetic recombinant human fibrils but the complexity of accessing to a binding site on human mutated fibrils produced in an animal model. In the search for an α-syn PET radiotracer, a very important and difficult point is to find one or several animal models that accurately reflect human pathology [10]. Negative results in the search for an α-syn PET imaging radiotracer highlight the challenges to overcome, particularly in terms of selectivity [13] and

predictivity of the models [10]. The gold-standard will always be evaluation in human tissue and, ultimately, *in vivo* in patients.

Gold-standard *in vitro* autoradiography experiments in *post-mortem* brain tissue of confirmed synucleinopathy cases, including PD and MSA, also failed to detect α-syn aggregates in Lewy bodies or glial cytoplasmic inclusions, respectively. Several hypotheses can be put forward to explain these negative results. Firstly, the size and density of the fibrils/aggregates: α-syn aggregates are much smaller in size and lower in density than Aβ plaques. In AD patient brain, Aβ plaques were 60-200 μm in diameter, while in PD brain Lewy neurites were only 30-40 μm (~5-fold smaller) [47, 48]. Lewy neurites were even thinner (<10 μm diameter), but rather long (~600 μm long) [49]. Glial cytoplasmic inclusions were 20-60 μm in diameter [50]. Density was clearly low in PD brain, with only 6 Lewy bodies that could be observed in one section (while there were more glial cytoplasmic inclusions in MSA brain), whereas more than a hundred Aβ plaques could be counted in one section of AD brain. Additionally, not all Aβ plaques were actually detected by [^{18}F]BF227. So there seem to be some Aβ plaques that do not have all characteristics necessary for [^{18}F]BF227 to access its binding site. Alternatively, the Aβ plaques in one AD patient had different structures, enabling [^{18}F]BF227 to bind only to certain Aβ plaques. The same argument could be applied to α-syn radiotracers: that one good tracer is not able to bind to all α-syn Lewy bodies, making the discovery of an α-syn radiotracer even more challenging. It is, however, encouraging that some radiotracers do successfully target neuronal receptors present at even lower densities [6, 13]. The negative results obtained with human *post-mortem* brains highlight the second "gap" between the feasibility of imaging synthetic recombinant human fibrils and the complexity of accessing a binding site in human *post-mortem* brain.

The discrepancy between results obtained with, on the one hand, computational modeling and recombinant human fibrils *in vitro* in injected rats and, on the other hand, *in vivo* with *post-mortem* human brain tissue, casts doubt on the predictivity of computational modeling, on screening candidate molecules with recombinant human fibrils produced *in vitro,* and on evaluating candidate radiotracers with animal models that do not perfectly reflect the full pathology. To overcome this major issue, several strategies can be put forward. First, concerning computational modeling, the failure of the experimental studies compared to the *in silico* predictions may come from the use of an α-syn fibril model that did not reflect the *in vivo* pathophysiology, as most information on α-syn fibril structure comes only from fibrils produced *in vitro.* An interesting research axis would be to have access to fibril structures (NMR or cryo-EM) derived from patients. There may be an important gap between fibrillary polymorphisms obtained *in vitro* and those present in the brains of patients, because of both the maturation environment and the speed of aggregation. The second strategy would be to perform filter binding assays with human *post-mortem* brain homogenates, as this is the reference method for quantification purposes [11, 51-53]. Another approach would be to produce fibrillary strains of Aβ and α-syn by amplification of recombinant human peptides with patient material isolated from human samples, in order to control structural polymorphism.

CONCLUSION

After the chemical design of 10 molecules derived from three structural families, bioinformatics modelling tools enabled us to select two original benzoxazole candidate ligands that were successfully labeled with fluorine-18. Evaluation in rats demonstrated the ability of both radiolabeled molecules to non-selectively detect Aβ and α-syn recombinant human fibrils *in*

vitro. However, small-animal PET imaging in this rat model showed that, although both candidate radioligands were able to cross the blood-brain barrier, they failed to detect either Aβ or α-syn fibrils *in vivo*. Similarly, [^{18}F]2FBox and [^{18}F]4FBox were unable to detect Aβ or α-syn in transgenic mouse models of Alzheimer's (PDAPP) and Parkinson's (M83) disease. Finally, gold-standard *in vitro* autoradiography experiments in *post-mortem* brain tissue of confirmed synucleinopathy cases, including PD and MSA, also failed to detect α-syn aggregates in Lewy bodies or glial cytoplasmic inclusions, respectively. [^{18}F]2FBox and [^{18}F]4FBox are not suitable α-syn PET radiotracers. This study presented an experimental paradigm, theoretically adapted to the research of PET tracers for aggregated proteins, but that needs to be improved in terms of the predictivity of computational modeling in order to be ready for application in subsequent radiotracer candidates.

ABREVIATIONS

α-syn : alpha-synuclein; PET : positron emission tomography; PD : Parkinson disease; PDD : Parkinson disease with dementia; DLB : Dementia with Lewy bodies; MSA : Multiple system atrophy; BBB : Blood brain barrier; 3D : Three dimension; AD, Alzheimer's disease; TIP5P : 5-site transferable interaction potential; MOE : Molecular operating environment; Aβ42: amyloid-β 1-42; WFI : water for injection; ThS: Thioflavin S; Cpu : Caudate putamen; Tg : Transgenic; PBS: Phosphate Buffer Saline; BSA : Bovine serum albumin; IRW: INVEON Research Workplace; ROI : region of interest, TAC : Time activity curves , SUV : standardized uptake values; SUVR : standardized uptake values ratio; PMF : potential of mean force.

Supplementary Data:

Supplementary Figure S.1. Localization of the interaction site on one of the two protofibrils constituted of 18 α-synucleins (A). Potential of mean force (PMF) along reaction coordinate (0.1Å) for the 3 molecules, BF227, 4FBox and 2FBox, to access the docking site (B).

Supplementary Figure S.2 Transmission Electron Microscopy (TEM) images of Aβ 1-42 fibrils (A) and α-syn fibrils. Scale bars as noted.

Supplementary Figure S.3. *In vitro* binding assays of [^{18}F]BF227**.** (A) Saturation binding curve for [^{18}F]BF227 specific binding to α-syn fibrils. (B) Saturation binding curve for [^{18}F]BF227 specific binding to Aβ 1-42 fibrils.

Supplementary Figure S.4. *Ex vivo* autoradiography performed with [^{18}F]BF227 and [^{18}F]2FBox showing the ability of the tracers to non-selectively detect Aβ42 and α-syn.

ACKNOWLEDGMENTS

Dr Mathieu Verdurand was supported by a Young Researcher Grant from the Fondation Plan Alzheimer (Alzheimer Plan 2008-2017). This work was performed within the framework of the LABEX PRIMES (ANR-11-LABX-0063) of Lyon University, as part of the "Investissements d'Avenir" program (ANR-11-IDEX-0007) of the French National Research Agency (ANR). Dr Thierry Baron of the French Agency for Food, Environmental and Occupational Health & Safety (ANSES) is thanked for the generous gift of the transgenic M83 mouse model. Dr Nicolas Rama is thanked for the generous gift of the transgenic PDAPP mouse model. Dr Claire Troakes, of London Degenerative Brain Bank, is also thanked for her assistance in accessing human postmortem patient brain tissue. We thank all patients and their families for consent to use tissues in research.

Conflict of Interest Statement

All authors declare that they have no conflict of interest.

REFERENCES

1. Golde, T. E.; Borchelt, D. R.; Giasson, B. I.; Lewis, J. Thinking laterally about neurodegenerative proteinopathies. *The Journal of clinical investigation* **2013,** *123*, 1847-55.
2. Surguchov, A. Intracellular Dynamics of Synucleins: "Here, There and Everywhere". *Int Rev Cell Mol Biol* **2015,** *320*, 103-69.
3. Baucknehtt, M.; Arnaldi, D.; Nobili, F.; Aarsland, D.; Morbelli, S. New tracers and new perspectives for molecular imaging in Lewy body diseases. *Curr Med Chem* **2017**.
4. McKeith, I. G.; Boeve, B. F.; Dickson, D. W.; Halliday, G.; Taylor, J. P.; Weintraub, D.; Aarsland, D.; Galvin, J.; Attems, J.; Ballard, C. G.; Bayston, A.; Beach, T. G.; Blanc, F.; Bohnen, N.; Bonanni, L.; Bras, J.; Brundin, P.; Burn, D.; Chen-Plotkin, A.; Duda, J. E.; El-Agnaf, O.; Feldman, H.; Ferman, T. J.; Ffytche, D.; Fujishiro, H.; Galasko, D.; Goldman, J. G.; Gomperts, S. N.; Graff-Radford, N. R.; Honig, L. S.; Iranzo, A.; Kantarci, K.; Kaufer, D.; Kukull, W.; Lee, V. M. Y.; Leverenz, J. B.; Lewis, S.; Lippa, C.; Lunde, A.; Masellis, M.; Masliah, E.; McLean, P.; Mollenhauer, B.; Montine, T. J.; Moreno, E.; Mori, E.; Murray, M.; O'Brien, J. T.; Orimo, S.; Postuma, R. B.; Ramaswamy, S.; Ross, O. A.; Salmon, D. P.; Singleton, A.; Taylor, A.; Thomas, A.; Tiraboschi, P.; Toledo, J. B.; Trojanowski, J. Q.; Tsuang, D.; Walker, Z.; Yamada, M.; Kosaka, K. Diagnosis and management of dementia with Lewy bodies: Fourth consensus report of the DLB Consortium. *Neurology* **2017,** *89*, 88-100.
5. M J Fox Fundation, ALPHA–SYNUCLEIN IMAGING PRIZE. https://www.michaeljfox.org/research/imaging-prize.html?navid=alpha-syn-image-prize (2018),
6. Eberling, J. L.; Dave, K. D.; Frasier, M. A. alpha-synuclein imaging: a critical need for Parkinson's disease research. *Journal of Parkinson's disease* **2013,** *3*, 565-7.
7. Kotzbauer, P. T.; Cairns, N. J.; Campbell, M. C.; Willis, A. W.; Racette, B. A.; Tabbal, S. D.; Perlmutter, J. S. Pathologic accumulation of alpha-synuclein and Abeta in Parkinson disease patients with dementia. *Archives of neurology* **2012,** *69*, 1326-31.
8. Trojanowski, J. Q. "Emerging Alzheimer's disease therapies: focusing on the future". *Neurobiology of aging* **2002,** *23*, 985-90.
9. McKeith, I. G.; Dickson, D. W.; Lowe, J.; Emre, M.; O'Brien, J. T.; Feldman, H.; Cummings, J.; Duda, J. E.; Lippa, C.; Perry, E. K.; Aarsland, D.; Arai, H.; Ballard, C. G.; Boeve, B.; Burn, D. J.; Costa, D.; Del Ser, T.; Dubois, B.; Galasko, D.; Gauthier, S.; Goetz, C. G.; Gomez-Tortosa, E.; Halliday, G.; Hansen, L. A.; Hardy, J.; Iwatsubo, T.; Kalaria, R. N.; Kaufer, D.; Kenny, R. A.; Korczyn, A.; Kosaka, K.; Lee, V. M.; Lees, A.; Litvan, I.; Londos, E.; Lopez, O. L.; Minoshima, S.; Mizuno, Y.; Molina, J. A.; Mukaetova-Ladinska, E. B.; Pasquier, F.; Perry, R. H.; Schulz, J. B.; Trojanowski, J. Q.; Yamada, M.; Consortium on, D. L. B. Diagnosis and management of dementia with Lewy bodies: third report of the DLB Consortium. *Neurology* **2005,** *65*, 1863-72.
10. Neal, K. L.; Shakerdge, N. B.; Hou, S. S.; Klunk, W. E.; Mathis, C. A.; Nesterov, E. E.; Swager, T. M.; McLean, P. J.; Bacskai, B. J. Development and screening of contrast agents for in vivo imaging of Parkinson's disease. *Molecular imaging and biology : MIB : the official publication of the Academy of Molecular Imaging* **2013,** *15*, 585-95.
11. Fodero-Tavoletti, M. T.; Mulligan, R. S.; Okamura, N.; Furumoto, S.; Rowe, C. C.; Kudo, Y.; Masters, C. L.; Cappai, R.; Yanai, K.; Villemagne, V. L. In vitro characterisation of BF227 binding to alpha-synuclein/Lewy bodies. *European journal of pharmacology* **2009,** *617*, 54-8.
12. Kikuchi, A.; Takeda, A.; Okamura, N.; Tashiro, M.; Hasegawa, T.; Furumoto, S.; Kobayashi, M.; Sugeno, N.; Baba, T.; Miki, Y.; Mori, F.; Wakabayashi, K.; Funaki, Y.; Iwata,

R.; Takahashi, S.; Fukuda, H.; Arai, H.; Kudo, Y.; Yanai, K.; Itoyama, Y. In vivo visualization of alpha-synuclein deposition by carbon-11-labelled 2-[2-(2-dimethylaminothiazol-5-yl)ethenyl]-6-[2-(fluoro)ethoxy]benzoxazole positron emission tomography in multiple system atrophy. *Brain : a journal of neurology* **2010,** *133*, 1772-8.

13. Bagchi, D. P.; Yu, L.; Perlmutter, J. S.; Xu, J.; Mach, R. H.; Tu, Z.; Kotzbauer, P. T. Binding of the radioligand SIL23 to alpha-synuclein fibrils in Parkinson disease brain tissue establishes feasibility and screening approaches for developing a Parkinson disease imaging agent. *PloS one* **2013,** *8*, e55031.

14. Chu, W.; Zhou, D.; Gaba, V.; Liu, J.; Li, S.; Peng, X.; Xu, J.; Dhavale, D.; Bagchi, D. P.; d'Avignon, A.; Shakerdge, N. B.; Bacskai, B. J.; Tu, Z.; Kotzbauer, P. T.; Mach, R. H. Design, Synthesis, and Characterization of 3-(Benzylidene)indolin-2-one Derivatives as Ligands for alpha-Synuclein Fibrils. *J Med Chem* **2015,** *58*, 6002-17.

15. Lansbury, P. T., Justman, C.J. Imaging of alpha-synuclein. 2009.

16. Lee, J. H.; Lee, I. H.; Choe, Y. J.; Kang, S.; Kim, H. Y.; Gai, W. P.; Hahn, J. S.; Paik, S. R. Real-time analysis of amyloid fibril formation of alpha-synuclein using a fibrillation-state-specific fluorescent probe of JC-1. *The Biochemical journal* **2009,** *418*, 311-23.

17. Ribeiro Morais, G.; Vicente Miranda, H.; Santos, I. C.; Santos, I.; Outeiro, T. F.; Paulo, A. Synthesis and in vitro evaluation of fluorinated styryl benzazoles as amyloid-probes. *Bioorganic & medicinal chemistry* **2011,** *19*, 7698-710.

18. Watanabe, H.; Ariyoshi, T.; Ozaki, A.; Ihara, M.; Ono, M.; Saji, H. Synthesis and biological evaluation of novel radioiodinated benzimidazole derivatives for imaging alpha-synuclein aggregates. *Bioorganic & medicinal chemistry* **2017,** *25*, 6398-6403.

19. Sgourakis, N. G.; Yau, W. M.; Qiang, W. Modeling an in-register, parallel "iowa" abeta fibril structure using solid-state NMR data from labeled samples with rosetta. *Structure* **2015,** *23*, 216-27.

20. Dearborn, A. D.; Wall, J. S.; Cheng, N.; Heymann, J. B.; Kajava, A. V.; Varkey, J.; Langen, R.; Steven, A. C. alpha-Synuclein Amyloid Fibrils with Two Entwined, Asymmetrically Associated Protofibrils. *J Biol Chem* **2016,** *291*, 2310-8.

21. Paxinos, G.; Watson, C., *The rat brain in stereotaxic coordinates*. 6, illustrated ed.; Academic Press, 2007: 2007; p 456 pages.

22. Mougenot, A. L.; Nicot, S.; Bencsik, A.; Morignat, E.; Verchere, J.; Lakhdar, L.; Legastelois, S.; Baron, T. Prion-like acceleration of a synucleinopathy in a transgenic mouse model. *Neurobiology of aging* **2012,** *33*, 2225-8.

23. Mucke, L.; Masliah, E.; Yu, G. Q.; Mallory, M.; Rockenstein, E. M.; Tatsuno, G.; Hu, K.; Kholodenko, D.; Johnson-Wood, K.; McConlogue, L. High-level neuronal expression of abeta 1-42 in wild-type human amyloid protein precursor transgenic mice: synaptotoxicity without plaque formation. *J Neurosci* **2000,** *20*, 4050-8.

24. Lancelot, S.; Roche, R.; Slimen, A.; Bouillot, C.; Levigoureux, E.; Langlois, J. B.; Zimmer, L.; Costes, N. A multi-atlas based method for automated anatomical rat brain MRI segmentation and extraction of PET activity. *PloS one* **2014,** *9*, e109113.

25. Thie, J. A. Understanding the standardized uptake value, its methods, and implications for usage. *J Nucl Med* **2004,** *45*, 1431-4.

26. Verdurand, M.; Chauveau, F.; Daoust, A.; Morel, A. L.; Bonnefoi, F.; Liger, F.; Berod, A.; Zimmer, L. Differential effects of amyloid-beta 1-40 and 1-42 fibrils on 5-HT1A serotonin receptors in rat brain. *Neurobiology of aging* **2016,** *40*, 11-21.

27. Pike, V. W. PET radiotracers: crossing the blood-brain barrier and surviving metabolism. *Trends Pharmacol Sci* **2009,** *30*, 431-40.

28. Kovacs, G. G.; Wagner, U.; Dumont, B.; Pikkarainen, M.; Osman, A. A.; Streichenberger, N.; Leisser, I.; Verchere, J.; Baron, T.; Alafuzoff, I.; Budka, H.; Perret-Liaudet, A.; Lachmann, I. An antibody with high reactivity for disease-associated alpha-synuclein reveals extensive brain pathology. *Acta neuropathologica* **2012,** *124*, 37-50.
29. Peelaerts, W.; Baekelandt, V. a-Synuclein strains and the variable pathologies of synucleinopathies. *J Neurochem* **2016,** *139 Suppl 1*, 256-274.
30. Vilar, M.; Chou, H. T.; Luhrs, T.; Maji, S. K.; Riek-Loher, D.; Verel, R.; Manning, G.; Stahlberg, H.; Riek, R. The fold of alpha-synuclein fibrils. *Proc Natl Acad Sci U S A* **2008,** *105*, 8637-42.
31. Tuttle, M. D.; Comellas, G.; Nieuwkoop, A. J.; Covell, D. J.; Berthold, D. A.; Kloepper, K. D.; Courtney, J. M.; Kim, J. K.; Barclay, A. M.; Kendall, A.; Wan, W.; Stubbs, G.; Schwieters, C. D.; Lee, V. M.; George, J. M.; Rienstra, C. M. Solid-state NMR structure of a pathogenic fibril of full-length human alpha-synuclein. *Nat Struct Mol Biol* **2016,** *23*, 409-15.
32. Balamurugan, K.; Murugan, N. A.; Agren, H. Multistep Modeling Strategy To Improve the Binding Affinity Prediction of PET Tracers to Abeta42: Case Study with Styrylbenzoxazole Derivatives. *ACS Chem Neurosci* **2016,** *7*, 1698-1705.
33. Poncin-Epaillard, F.; Mille, C.; Debarnot, D.; Zorzi, W.; El Moualij, B.; Coudreuse, A.; Legeay, G.; Quadrio, I.; Perret-Liaudet, A. Study of the adhesion of neurodegenerative proteins on plasma-modified and coated polypropylene surfaces. *J Biomater Sci Polym Ed* **2012,** *23*, 1879-93.
34. Vrlinic, T.; Debarnot, D.; Legeay, G.; Coudreuse, A.; El Moualij, B.; Zorzi, W.; Perret-Liaudet, A.; Quadrio, I.; Mozetic, M.; Poncin-Epaillard, F. Are the interactions between recombinant prion proteins and polymeric surfaces related to the hydrophilic/hydrophobic balance? *Macromol Biosci* **2012,** *12*, 830-9.
35. Bousset, L.; Pieri, L.; Ruiz-Arlandis, G.; Gath, J.; Jensen, P. H.; Habenstein, B.; Madiona, K.; Olieric, V.; Bockmann, A.; Meier, B. H.; Melki, R. Structural and functional characterization of two alpha-synuclein strains. *Nat Commun* **2013,** *4*, 2575.
36. Petkova, A. T.; Leapman, R. D.; Guo, Z.; Yau, W. M.; Mattson, M. P.; Tycko, R. Self-propagating, molecular-level polymorphism in Alzheimer's beta-amyloid fibrils. *Science* **2005,** *307*, 262-5.
37. Prusiner, S. B.; Woerman, A. L.; Mordes, D. A.; Watts, J. C.; Rampersaud, R.; Berry, D. B.; Patel, S.; Oehler, A.; Lowe, J. K.; Kravitz, S. N.; Geschwind, D. H.; Glidden, D. V.; Halliday, G. M.; Middleton, L. T.; Gentleman, S. M.; Grinberg, L. T.; Giles, K. Evidence for alpha-synuclein prions causing multiple system atrophy in humans with parkinsonism. *Proc Natl Acad Sci U S A* **2015,** *112*, E5308-17.
38. Kherlopian, A. R.; Song, T.; Duan, Q.; Neimark, M. A.; Po, M. J.; Gohagan, J. K.; Laine, A. F. A review of imaging techniques for systems biology. *BMC Syst Biol* **2008,** *2*, 74.
39. Johnstrom, P.; Bird, J. L.; Davenport, A. P. Quantitative phosphor imaging autoradiography of radioligands for positron emission tomography. *Methods Mol Biol* **2012,** *897*, 205-20.
40. Maeda, J.; Ji, B.; Irie, T.; Tomiyama, T.; Maruyama, M.; Okauchi, T.; Staufenbiel, M.; Iwata, N.; Ono, M.; Saido, T. C.; Suzuki, K.; Mori, H.; Higuchi, M.; Suhara, T. Longitudinal, quantitative assessment of amyloid, neuroinflammation, and anti-amyloid treatment in a living mouse model of Alzheimer's disease enabled by positron emission tomography. *J Neurosci* **2007,** *27*, 10957-68.
41. Klunk, W. E.; Lopresti, B. J.; Ikonomovic, M. D.; Lefterov, I. M.; Koldamova, R. P.; Abrahamson, E. E.; Debnath, M. L.; Holt, D. P.; Huang, G. F.; Shao, L.; DeKosky, S. T.; Price, J.

C.; Mathis, C. A. Binding of the positron emission tomography tracer Pittsburgh compound-B reflects the amount of amyloid-beta in Alzheimer's disease brain but not in transgenic mouse brain. *J Neurosci* **2005,** *25*, 10598-606.
42. Toyama, H.; Ye, D.; Ichise, M.; Liow, J. S.; Cai, L.; Jacobowitz, D.; Musachio, J. L.; Hong, J.; Crescenzo, M.; Tipre, D.; Lu, J. Q.; Zoghbi, S.; Vines, D. C.; Seidel, J.; Katada, K.; Green, M. V.; Pike, V. W.; Cohen, R. M.; Innis, R. B. PET imaging of brain with the beta-amyloid probe, [11C]6-OH-BTA-1, in a transgenic mouse model of Alzheimer's disease. *Eur J Nucl Med Mol Imaging* **2005,** *32*, 593-600.
43. Furumoto, S.; Okamura, N.; Iwata, R.; Yanai, K.; Arai, H.; Kudo, Y. Recent advances in the development of amyloid imaging agents. *Curr Top Med Chem* **2007,** *7*, 1773-89.
44. Okamura, N.; Suemoto, T.; Shimadzu, H.; Suzuki, M.; Shiomitsu, T.; Akatsu, H.; Yamamoto, T.; Staufenbiel, M.; Yanai, K.; Arai, H.; Sasaki, H.; Kudo, Y.; Sawada, T. Styrylbenzoxazole derivatives for in vivo imaging of amyloid plaques in the brain. *J Neurosci* **2004,** *24*, 2535-41.
45. Levigoureux, E.; Lancelot, S.; Bouillot, C.; Chauveau, F.; Verdurand, M.; Verchere, J.; Billard, T.; Baron, T.; Zimmer, L. Binding of the PET radiotracer [(1)(8)F]BF227 does not reflect the presence of alpha-synuclein aggregates in transgenic mice. *Current Alzheimer research* **2014,** *11*, 955-60.
46. Zimmer, L.; Luxen, A. PET radiotracers for molecular imaging in the brain: past, present and future. *Neuroimage* **2012,** *61*, 363-70.
47. Irvine, G. B.; El-Agnaf, O. M.; Shankar, G. M.; Walsh, D. M. Protein aggregation in the brain: the molecular basis for Alzheimer's and Parkinson's diseases. *Mol Med* **2008,** *14*, 451-64.
48. Anderson, V. L.; Webb, W. W. Transmission electron microscopy characterization of fluorescently labelled amyloid beta 1-40 and alpha-synuclein aggregates. *BMC Biotechnol* **2011,** *11*, 125.
49. Seidel, K.; Mahlke, J.; Siswanto, S.; Kruger, R.; Heinsen, H.; Auburger, G.; Bouzrou, M.; Grinberg, L. T.; Wicht, H.; Korf, H. W.; den Dunnen, W.; Rub, U. The brainstem pathologies of Parkinson's disease and dementia with Lewy bodies. *Brain Pathol* **2015,** *25*, 121-35.
50. Cykowski, M. D.; Coon, E. A.; Powell, S. Z.; Jenkins, S. M.; Benarroch, E. E.; Low, P. A.; Schmeichel, A. M.; Parisi, J. E. Expanding the spectrum of neuronal pathology in multiple system atrophy. *Brain : a journal of neurology* **2015,** *138*, 2293-309.
51. Fodero-Tavoletti, M. T.; Smith, D. P.; McLean, C. A.; Adlard, P. A.; Barnham, K. J.; Foster, L. E.; Leone, L.; Perez, K.; Cortes, M.; Culvenor, J. G.; Li, Q. X.; Laughton, K. M.; Rowe, C. C.; Masters, C. L.; Cappai, R.; Villemagne, V. L. In vitro characterization of Pittsburgh compound-B binding to Lewy bodies. *J Neurosci* **2007,** *27*, 10365-71.
52. Choi, S. R.; Schneider, J. A.; Bennett, D. A.; Beach, T. G.; Bedell, B. J.; Zehntner, S. P.; Krautkramer, M. J.; Kung, H. F.; Skovronsky, D. M.; Hefti, F.; Clark, C. M. Correlation of amyloid PET ligand florbetapir F 18 binding with Abeta aggregation and neuritic plaque deposition in postmortem brain tissue. *Alzheimer Dis Assoc Disord* **2012,** *26*, 8-16.
53. Ikonomovic, M. D.; Klunk, W. E.; Abrahamson, E. E.; Mathis, C. A.; Price, J. C.; Tsopelas, N. D.; Lopresti, B. J.; Ziolko, S.; Bi, W.; Paljug, W. R.; Debnath, M. L.; Hope, C. E.; Isanski, B. A.; Hamilton, R. L.; DeKosky, S. T. Post-mortem correlates of in vivo PiB-PET amyloid imaging in a typical case of Alzheimer's disease. *Brain : a journal of neurology* **2008,** *131*, 1630-45.

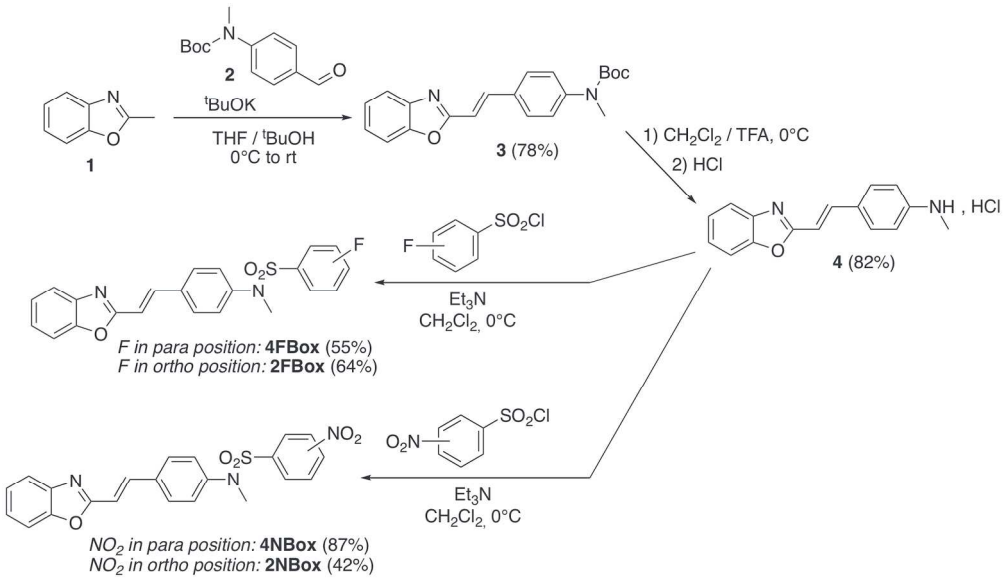

Figure 1. Diagram of the chemical syntheses of the non-radioactive FBox compounds and their precursors (Nbox) for radiosyntheses.

196x112mm (300 x 300 DPI)

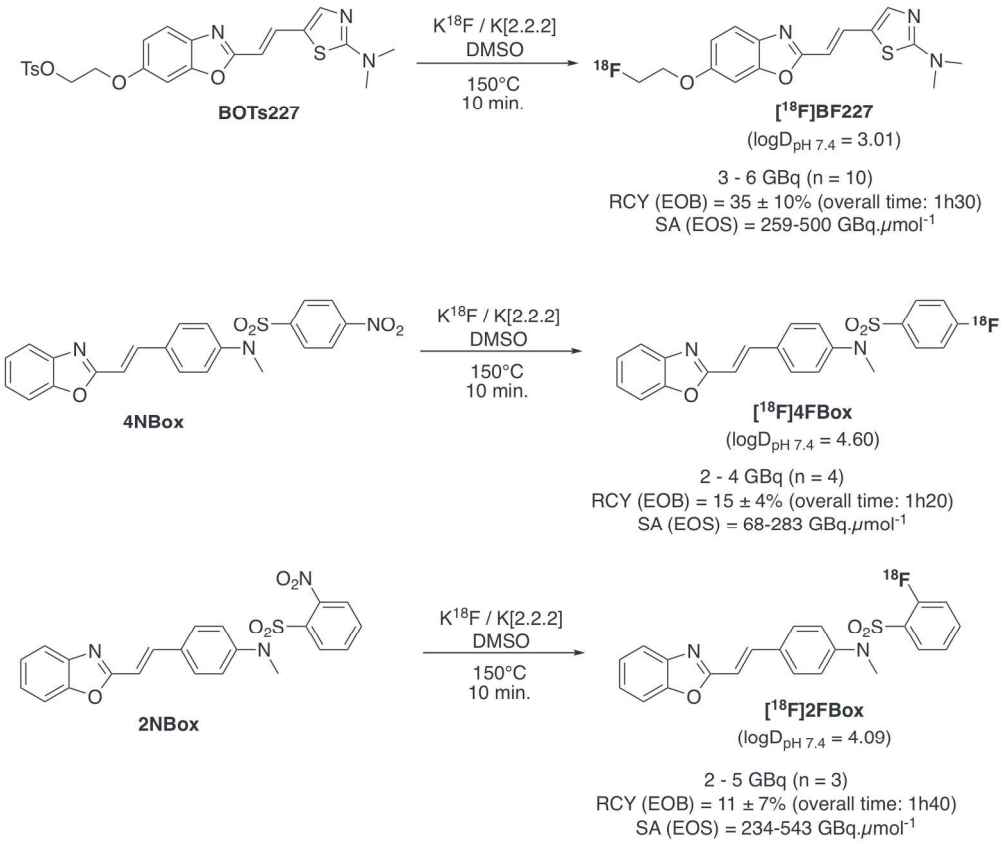

Figure 2. Diagram of the radiosynthesis of [18F]BF227 (A), [18F]4FBox (B) and [18F]2FBox (C). RCY data are mean±SD values.

182x153mm (300 x 300 DPI)

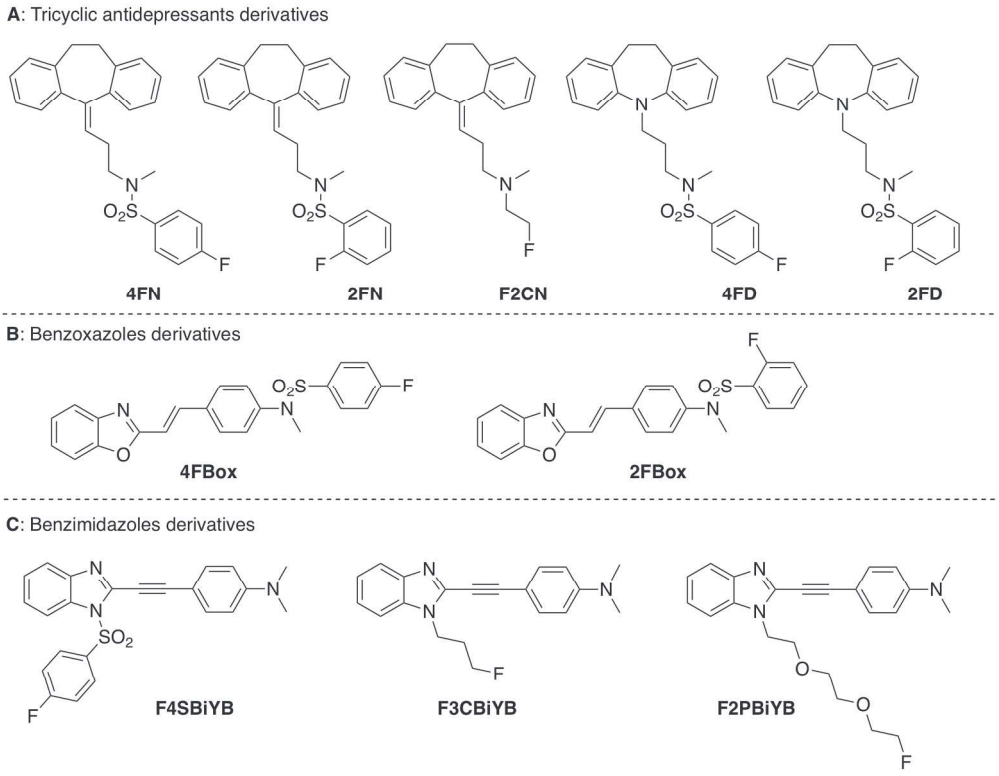

Figure 3. Diagram of the 10 molecules derived from three structural families with (1A) the antidepressant tricyclic derivatives, (1B) the benzoxazoles derivatives and (1C) the benzimidazoles derivatives.

189x145mm (300 x 300 DPI)

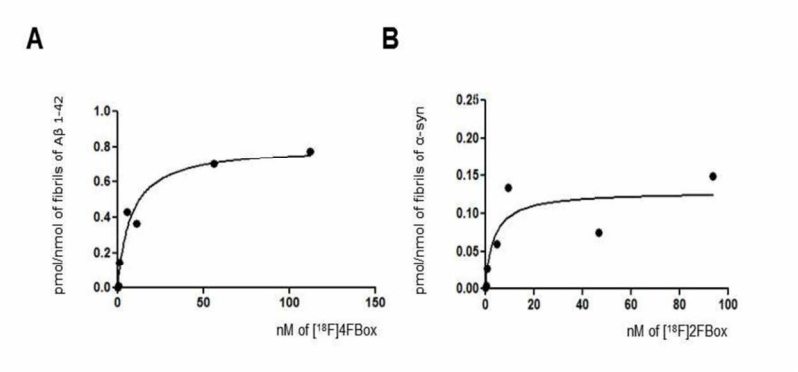

Figure 4. In vitro binding assays. (A) Saturation binding curve for [18F]4FBox specific binding to Aβ42 fibrils. (B) Saturation binding curve for [18F]2FBox specific binding to α-syn fibrils.

127x95mm (300 x 300 DPI)

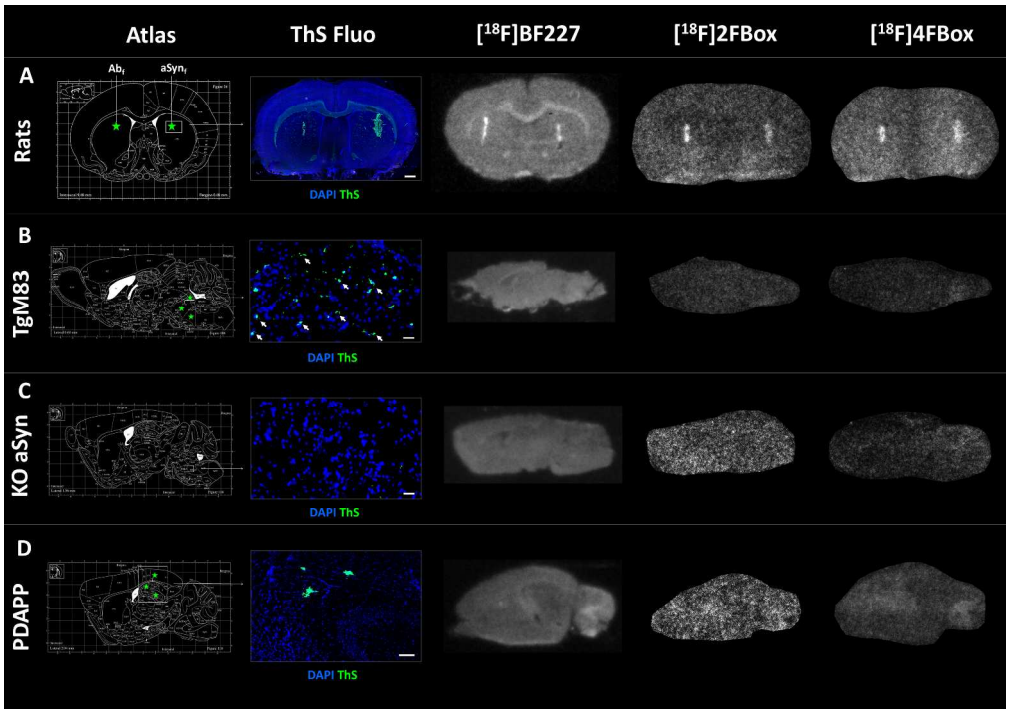

Figure 5. In vitro autoradiography with [18F]BF227, [18F]2FBox and [18F]4FBox in animal models. (A) fibril-injected rats; (B) M83 transgenic mice expressing human mutated form of α-syn; (C) α-syn knock-out transgenic mouse model; and (D) PDAPP transgenic mouse model overexpressing 2 mutated forms of human amyloid precursor protein. On the left, stereotaxic atlas figures of the anatomical level represented in the various animal models (green stars indicate fibril injection sites). Green ThS fluorescence images illustrate the localization (white arrows) and confirm the presence of α-syn and Aβ aggregates in the various animal models (DAPI blue fluorescence indicates cell nuclei). Scale bars represent 200 µm in rats and PDAPP mice, and 20 µm in M83 and α-syn KO mice.

1418x997mm (55 x 55 DPI)

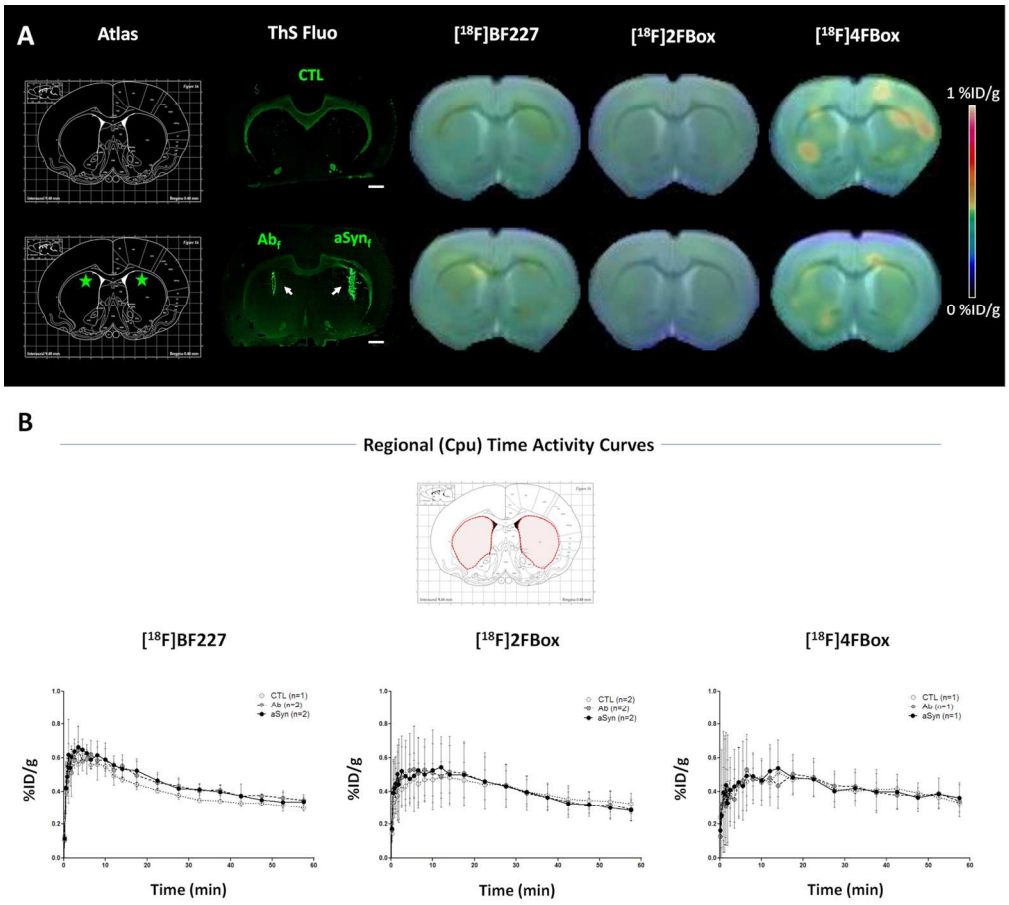

Figure 6. Small-animal PET imaging with [18F]BF227, [18F]2FBox and [18F]4FBox in control and fibril-injected rats. (A) Summed PET images were co-registered with CT images and radioactivity index was reflected by a color scale representing %ID/g. Thioflavin S fluorescence staining of Aβ42 and α-syn fibrils injected in the striata is presented (white arrows), with the corresponding stereotaxic brain atlas region (green stars representing injection sites). Scale bar represent 1 mm on ThS fluorescence staining. (B) Time activity curves (expressed in %ID/g over time) for each radiotracer are presented. Values (mean ± SD) were extracted from the striata regions thanks to an in-house made MRI atlas that was co-registered to PET-CT images.

169x169mm (300 x 300 DPI)

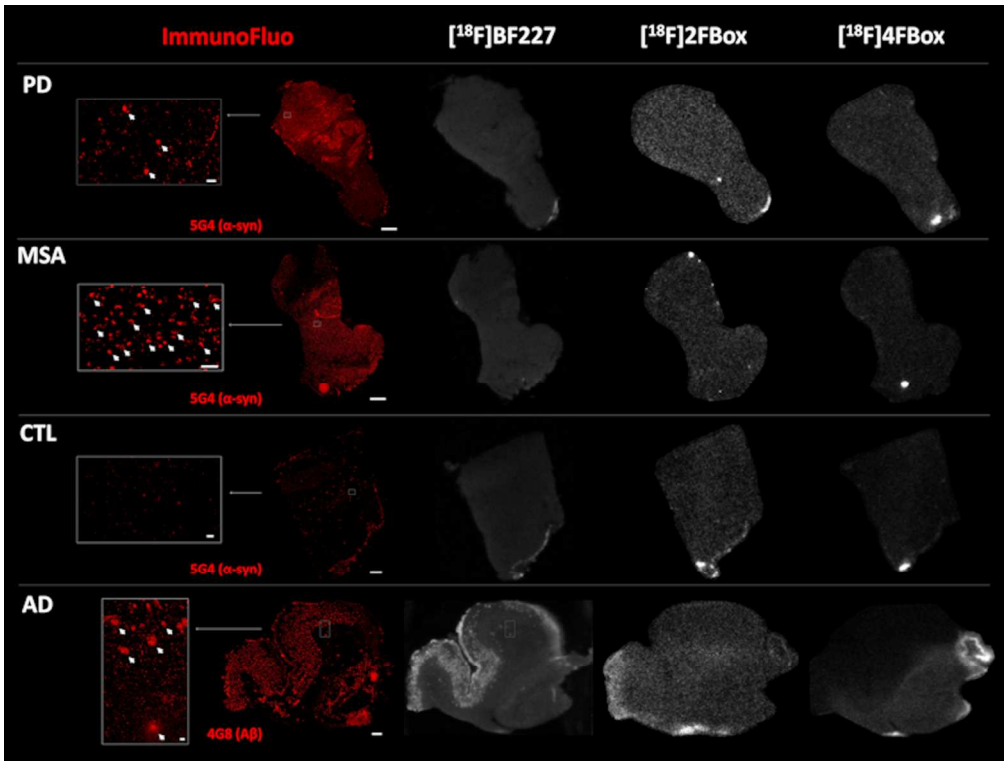

Figure 7. In vitro autoradiography with [18F]BF227, [18F]2FBox and [18F]4FBox in postmortem human brain. (A) PD patient, (B) MSA patient and (C) control patient medulla oblongata, and (D) AD patient cortex and hippocampus region. Left: immunofluorescence staining with α-syn proteins labeled with 5G4 antibody, and Aβ proteins with 4G8 antibody (white arrows). Scale bars in the zoom box represent 50 µm in PD, MSA and CTL, and 100 µm in AD brain. In the digitized whole-brain sections, scale bars represent 2 mm. Note that only [18F]BF227 was able to label Aβ plaques in the AD patient, as demonstrated by the co-localization of [18F]BF227 radioactive signal (in white) and 4G8 immunostaining (in red).

136x103mm (300 x 300 DPI)

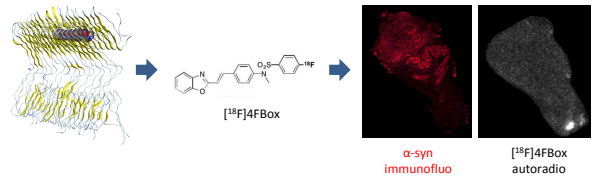
[18F]4FBox
α-syn
immunofluo
[18F]4FBox
autoradio
Identified docking site
in α-syn fibril model
Original radioligand
developped
BUT no binding to α-syn in
Parkinson's post-mortem brain